

# ROLE OF EJECTA CLUMPING AND BACK-REACTION OF ACCELERATED COSMIC RAYS IN THE EVOLUTION OF TYPE IA SUPERNOVA REMNANTS

S. ORLANDO<sup>1</sup>, F. BOCCHINO<sup>1</sup>, M. MICELI<sup>2,1</sup>, O. PETRUK<sup>3,4</sup>, M.L. PUMO<sup>5,6</sup>

## ABSTRACT

We investigate the role played by initial clumping of ejecta and by efficient acceleration of cosmic rays (CRs) in determining the density structure of the post-shock region of a Type Ia supernova remnant (SNR) through detailed 3D MHD modeling. Our model describes the expansion of a SNR through a magnetized interstellar medium (ISM), including the initial clumping of ejecta and the effects on shock dynamics due to back-reaction of accelerated CRs. The model predictions are compared to the observations of SN 1006. We found that the back-reaction of accelerated CRs alone cannot reproduce the observed separation between the forward shock (FS) and the contact discontinuity (CD) unless the energy losses through CR acceleration and escape are very large and independent of the obliquity angle. On the contrary, the clumping of ejecta can naturally reproduce the observed small separation and the occurrence of protrusions observed in SN 1006, even without the need of accelerated CRs. We conclude that FS-CD separation is a probe of the ejecta structure at the time of explosion rather than a probe of the efficiency of CR acceleration in young SNRs.

*Subject headings:* cosmic rays — magnetohydrodynamics (MHD) — instabilities — shock waves — ISM: supernova remnants — supernovae: individual: SN 1006

## 1. INTRODUCTION

Nowadays it is widely accepted that supernova remnants (SNRs) are the site where cosmic ray (CR) diffusive shock acceleration occurs. Observations in various bands support this picture through the detection of non-thermal emission that is compatible with being synchrotron or Inverse Compton radiation from CR electrons. Unfortunately, the direct evidence of CR ions in SNRs is difficult to find because they do not radiate efficiently. On the other hand, different indirect signatures of the presence of CR ions are largely discussed in the literature. The most popular is probably the separation between the forward shock and the contact discontinuity that has been measured in young SNRs (e.g. SN 1006, Miceli et al. 2009, and Tycho's SNR, Warren et al. 2005; Cassam-Chenaï et al. 2007). In fact, current theories predict that a significant fraction of the energy of supernova remnant shocks is channeled into CRs, determining modifications of the shock dynamics that depend on the efficiency of acceleration and injection processes of high energy particles. In particular, this energy losses would lead to a greater shock compression ratio and, as a consequence, to a thinner shell of shocked interstellar medium (ISM).

An example of SNR in which the observed features have been interpreted as a consequence of the energy losses to CRs at the forward shock is SN 1006. In this

remnant, the observations have shown that the azimuthal profile of the ratio of the forward shock radius to the contact discontinuity radius  $R_{fs}/R_{cd}$  is fairly uniform (although very noisy) and much lower than predicted for a non-modified shock (Miceli et al. 2009). Recently Rakowski et al. (2011) have found and analyzed clumps of ejecta close to or protruding beyond the main blast wave of SN 1006 that have been interpreted in the context of an upstream medium modified by the saturated nonresonant Bell instability which enhances the growth of Rayleigh-Taylor (RT) instabilities at the contact discontinuity.

However, some pieces of evidence are now accumulating that are difficult to explain in terms of acceleration of CR particles. Some authors (e.g. Blondin & Ellison 2001; Wang 2011 and references therein) noted that extreme energy losses to accelerate the CRs are needed to allow a significant fraction of the ejecta to approach or even overtake the forward shock, thus explaining the thin shell of shocked ISM. Wang (2011) analyzed the evolution of RT instabilities in Type Ia SNRs undergoing CR particle acceleration and found that, even with very efficient acceleration of CRs (i.e. assuming an effective adiabatic index  $\gamma_{eff} \approx 1.1$ ), significantly enhanced mixing and perturbation of the remnant outline are not expected. A similar conclusion was reached by Frascchetti et al. (2010) who found that the development of RT instabilities in SNRs is not drastically affected by CR particle acceleration. In addition, these studies suggest that the high occurrence of protrusions in young SNRs is not the consequence of RT instabilities enhanced by accelerated CRs (see also Wang & Chevalier 2001). Another evidence difficult to explain in terms of acceleration of CR particles is the ratio  $R_{fs}/R_{cd}$  measured in SN 1006 that is lower than predicted by non-modified shock models even in regions dominated by thermal emission where the CR acceleration efficiency is supposed to be low (e.g. Miceli et al. 2009). All these studies cast some doubts on whether the back-reaction of accelerated CRs is the main respon-

Electronic address: orlando@astropa.inaf.it

<sup>1</sup> INAF - Osservatorio Astronomico di Palermo "G.S. Vaiana", Piazza del Parlamento 1, 90134 Palermo, Italy

<sup>2</sup> Dip. di Fisica, Univ. di Palermo, Piazza del Parlamento 1, 90134 Palermo, Italy

<sup>3</sup> Institute for Applied Problems in Mechanics and Mathematics, Naukova St. 3-b Lviv 79060, Ukraine

<sup>4</sup> Astronomical Observatory, National University, Kyryla and Methodia St. 8 Lviv 79008, Ukraine

<sup>5</sup> INAF - Osservatorio Astronomico di Padova, Vicolo dell'Osservatorio 5, 35122 Padova, Italy

<sup>6</sup> INAF - Osservatorio Astrofisico di Catania, Via S. Sofia 78, 95123 Catania, Italy

sible of the enhanced intershock instabilities observed in young SNRs (e.g. SN 1006 and Tycho's SNR).

On the other hand, spectropolarimetric studies of SNe Ia show the presence of asymmetries with different magnitude and orientation for different elements in the ejecta and the detection of strong line polarization (e.g. Wang et al. 2003, 2004; Leonard et al. 2005; Wang et al. 2006; Chornock & Filippenko 2008; Hole et al. 2010). All these features have been interpreted as being due to clumpy structures in the outer layers of the ejecta (see Hole et al. 2010 and references therein) and some authors suggested that ejecta clumps of intermediate-mass elements can be forged in the explosion of SN Ia (e.g. Wang et al. 2003; Leonard et al. 2005) or may be due to the interaction of the ejecta with a dense, clumpy, and disk-like circumstellar environment (e.g. Wang et al. 2004). Recently Maeda et al. (2010a) have shown that asymmetries in the explosion can be a generic feature in SNe Ia (see also Maeda et al. 2010b), and these asymmetries, in turn, may lead to a clumpy structure of the ejecta. In the light of these considerations, it is therefore important to investigate the role of ejecta clumping on the evolution and morphology of Type Ia SNRs. In particular we wonder whether the thermal and density structure of the post-shock region of a young SNR originates mainly from the clumpy structure of the ejecta rather than as a consequence of back-reaction of accelerated CRs. The density inhomogeneities in the ejecta can enhance the growth of RT instabilities, causing the ejecta material to move closer to the main blast. The question is: can the ejecta clumping enhance the growth of RT instabilities up to a level that allows clumps of ejecta to reach and possibly overtake the forward shock?

Here we investigate this issue by developing a three-dimensional (3D) MHD model describing the expansion of a SNR through a magnetized medium, including, for the first time, the (non-uniform) ambient magnetic field, the initial ejecta clumping, and the effects on shock dynamics due to back-reaction of accelerated CRs. The paper is organized as follows: in Sect. 2 we describe the MHD model and the numerical setup; in Sect. 3 we describe the results and, finally, we draw our conclusions in Sect. 4.

## 2. MHD MODEL AND NUMERICAL SETUP

The evolution of a SNR can be characterized by distinct stages depending on the physical process dominating its dynamics (e.g. Chevalier 1977). This paper focuses on young SNRs, i.e. remnants that have evolved from the ejecta-dominated stage through the Sedov-Taylor stage. Pioneering comprehensive studies of the dynamics of these remnants, preceding the onset of dynamically significant radiative losses and/or pressure confinement by the ambient medium, are given in the literature (e.g. Mansfield & Salpeter 1974; Franco et al. 1994; Truelove & McKee 1999) and are mostly based on analytic and numerical 1D hydrodynamic models. Subsequently several 2D and 3D hydrodynamic and MHD models describing the evolution of the remnant through the ISM have been developed.

Here we adopted the 3D MHD model discussed by Orlando et al. (2007, 2011), extended to describe the initial ejecta clumping and to include the effect of larger compressibility of plasma around the shock due to the

back reaction of accelerated CRs. The shock propagation is modeled by numerically solving the time-dependent ideal MHD equations of mass, momentum, and energy conservation in a 3D cartesian coordinate system  $(x, y, z)$  (see Orlando et al. 2007 for details). In order to trace the motion of the ejecta material and study its dynamics, we considered a passive tracer associated with the ejecta. The continuity equation of the tracer is solved in addition to our set of MHD equations; the ejecta material is initialized with  $C_{ej} = 1$ , while  $C_{ej} = 0$  in the ISM. The calculations were performed using FLASH (Fryxell et al. 2000), an advanced multi-dimensional MHD code for astrophysical plasmas, including the adaptive mesh refinement through the PARAMESH library (MacNeice et al. 2000), and extended with additional computational modules to handle the back-reaction of accelerated CRs.

The effects of shock modification are included in the MHD model by following the approach of Ferrand et al. (2010) and extending their method to MHD models. In particular, our model includes an effective adiabatic index  $\gamma_{eff}$  which depends on the injection rate  $\eta$  of particles (i.e. the fraction of ISM particles entering the shock front). The adiabatic index on the shock is varied due to particle acceleration as in Ellison et al. (2004) (see also Ferrand et al. 2010). At each time-step of integration, the adiabatic index is calculated at the shock front and then is advected within the remnant, remaining constant in each fluid element. As discussed by Ferrand et al. (2010), the latter assumption implies that each fluid element remembers the effect of shock modification induced by particle acceleration at the time it was shocked.

For the purposes of the present paper, we assume that the maximum injection rate  $\eta$  is large enough (e.g.  $\eta \approx 10^{-3}$ , namely when shock modifications are strong and immediate) so that the effective adiabatic index at the initial conditions of our simulations has already reached its minimum value and slightly depends on time (Ferrand et al. 2010). We assume therefore the effective adiabatic index not depending on time and consider its minimum value  $\gamma_{min}$  as a free parameter. On the other hand, the injection rate is expected to depend on the shock obliquity (i.e. the angle between the unperturbed external magnetic field and the normal to the shock; e.g. Völk et al. 2003). We allow therefore that the effects of shock modification on the fluid dynamics (and, therefore, the effective adiabatic index) vary in space as a function of the obliquity angle. We assume no magnetic field amplification due to CRs, and no back-reaction of accelerated CRs at the reverse shock, although the suggestion that CR particles can be efficiently accelerated also at the reverse shock is largely debated in the literature (e.g. Ellison et al. 2005).

The index  $\gamma_{eff}$  is calculated at the shock front by using a parametrized function depending on the obliquity angle  $\Theta_o$  and characterized by a parameter representing the minimum value of the adiabatic index  $\gamma_{min}$  that is possible to reach during the simulation:

$$\gamma_{eff} = \gamma - (\gamma - \gamma_{min}) \times f_{\zeta}(\Theta_o) \quad (1)$$

where  $\gamma = 5/3$  is the adiabatic index and  $f_{\zeta}(\Theta_o)$  is a function defined in the range  $[0, 1]$  depending on the obliquity angle  $\Theta_o$  and describing the variations of  $\gamma_{eff}$  over the surface of the remnant shock. In analogy with

the description given by Fulbright & Reynolds (1990) for the quasi-parallel, quasi-perpendicular, and isotropic injection models (see also Orlando et al. 2007, 2011), we model the variations of  $\gamma_{\text{eff}}$  over the shock surface through the functions  $f_{\zeta}(\Theta_o) = \cos^2 \Theta_s$  (i.e.  $\gamma_{\text{eff}}$  is minimum at parallel shocks),  $f_{\zeta}(\Theta_o) = \sin^2 \Theta_s$  ( $\gamma_{\text{eff}}$  is minimum at perpendicular shocks), and  $f_{\zeta}(\Theta_o) = 1$  ( $\gamma_{\text{eff}}$  is uniform at the shock front and equal to its minimum value), where  $\Theta_s$  is the angle between the shock normal and the post-shock magnetic field and is related to  $\Theta_o$  by the expression  $\cos \Theta_s = \sigma^{-1} \cos \Theta_o$  and  $\sigma$  is the shock compression ratio. The first case follows the quasi-parallel injection scenario, leading to a 3D polar-caps structure of the remnant, whereas the second and the third cases follow the quasi-perpendicular and isotropic injection models, respectively, producing a 3D equatorial-belt structure of the remnant. Note that the third case (isotropic) is intended to be the extreme case in which the shock modification is the largest everywhere at the forward shock with no obliquity dependence.

As for the density structure of the ejecta, we investigated: the exponential profile that has been shown to be the most representative of explosion models for thermonuclear SNe (Dwarkadas & Chevalier 1998), and the power-law profile with index  $n = 7$  that has been used to represent deflagration models (Chevalier 1983; Nomoto et al. 1984). We also assume that the initial ejecta has a clumpy structure. The clumps have been modelled as per-cell random density perturbations<sup>7</sup> derived from a power-law probability distribution<sup>8</sup> (index  $n = -1$ ) that is characterized by a parameter  $\nu_{\text{max}}$  representing the maximum density perturbation allowed in the simulation. Figure 1 shows the power-law probability distributions of the perturbations used in this paper for the two ejecta density profiles considered. We explored maximum density perturbations ranging between 1.5 and 5; we explored density clumps of ejecta with size either 1% or 2% of the initial diameter of the remnant  $D_{\text{SNR}0}$ . As discussed in Sect. 3.2, initial clump size in the range explored here leads, after 1000 yr of evolution, to density features with characteristic size comparable to those observed in SN 1006.

It is interesting to note that the range of clump size investigated in this paper is also in agreement with that derived by Hole et al. (2010) for SNe Ia. In particular these authors compared the results of their semi-analytic code for modeling polarized line radiative transfer within 3D inhomogeneous rapidly expanding atmospheres with spectropolarimetric observations; they found that the model reproduces the observed range of values of peak line polarization if the clumps have radius in the range<sup>9</sup>

<sup>7</sup> The density perturbation of each clump is calculated as the ratio of the mass density of the resulting clump to the local average density in the region occupied by the clump if the perturbation was not present.

<sup>8</sup> Since no observational clues are available on the distribution of density perturbations of the clumps, it is reasonable to assume that most of the clumps are characterized by small density perturbations and few of them by large perturbations. To this end, for the sake of simplicity, we assume a power-law probability distribution with index  $n = -1$ .

<sup>9</sup> Sizes are given in velocities because of the linear dependence of velocity on distance in the homologous flow of SN ejecta (this structure is sometimes referred to as a pseudo-Hubble flow; see Hole et al. 2010).

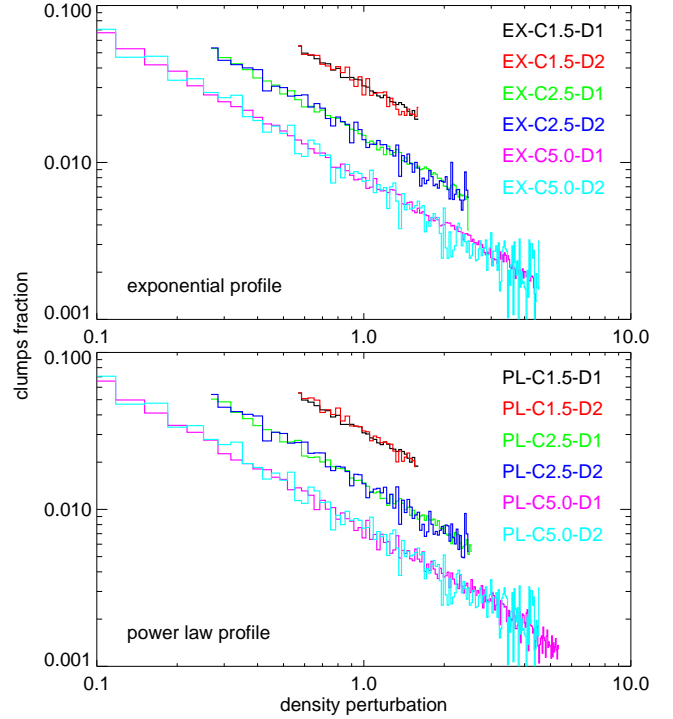


FIG. 1.— Probability distribution functions of the random perturbation of mass density of the clumps for the two ejecta density profiles considered in this paper: the exponential profile (upper panel) and the power-law profile with index  $n = 7$  (lower panel). The density perturbation of each clump is calculated as the ratio of the density of the resulting clump to the local average density in the region occupied by the clump if the perturbation was not present.

1000 – 6000 km s<sup>-1</sup>. At the time of our initial condition ( $\approx 10$  yr since the SN explosion), the effective range of clump size derived by Hole et al. (2010) corresponds to 0.016–0.13 pc to be compared with the size of the clumps modelled here ranging between 0.01 and 0.02 pc. As an example, Fig. 2 shows the initial spatial distribution of ejecta clumps for a model with the highest density perturbation and largest clump size. A summary of all the simulations discussed in this paper is given in Table 1.

Note that the ejecta clumps are presumably relics of the deflagration of the outer layers of the exploding star (as suggested by theoretical arguments and observations). In principle, therefore, the clumps are expected to be concentrated in a shell within the ballistically expanding ejecta rather than being distributed in the whole unshocked ejecta as done here. On the other hand, in our simulations, the ramp profile of the initial velocity of the ejecta makes the clumps in the outer layers those with the highest speed, so that the shocked ISM is mostly perturbed by such clumps. Concerning the focus of this paper, namely the structure of the RT mixing in the region between the forward and reverse shocks, we do not expect therefore significant changes to our results if considering a distribution of clumps concentrated in the outer layers of the ejecta.

As initial conditions, we adopted parameters appropriate to reproducing the SNR SN 1006 after 1000 yr of evolution: we assumed an initial spherical remnant with radius  $R_{\text{fs}0} = 0.5$  pc (corresponding to an initial age of  $\approx 10$  yr), originating in a progenitor star with mass of  $1.4 M_{\text{sun}}$ , and propagating through an unper-

TABLE 1  
ADOPTED PARAMETERS AND INITIAL CONDITIONS FOR THE MHD MODELS OF THE SNR

Model abbreviation	ejecta profile	ejecta clump.	shock mod.	$\nu_{\max}^a$	clump size <sup>b</sup>	injection efficiency	$\min(\gamma_{\text{eff}})$	initial age [yr]
REF-EX	EXP <sup>c</sup>	no	no	—	—	—	5/3	10
REF-PL	PLAW <sup>d</sup>	no	no	—	—	—	5/3	10
EX-C1.5-D1	EXP	yes	no	1.5	1%	—	5/3	10
EX-C1.5-D2	EXP	yes	no	1.5	2%	—	5/3	10
EX-C2.5-D1	EXP	yes	no	2.5	1%	—	5/3	10
EX-C2.5-D2	EXP	yes	no	2.5	2%	—	5/3	10
EX-C5.0-D1	EXP	yes	no	5.0	1%	—	5/3	10
EX-C5.0-D2	EXP	yes	no	5.0	2%	—	5/3	10
PL-C1.5-D1	PLAW	yes	no	1.5	1%	—	5/3	10
PL-C1.5-D2	PLAW	yes	no	1.5	2%	—	5/3	10
PL-C2.5-D1	PLAW	yes	no	2.5	1%	—	5/3	10
PL-C2.5-D2	PLAW	yes	no	2.5	2%	—	5/3	10
PL-C5.0-D1	PLAW	yes	no	5.0	1%	—	5/3	10
PL-C5.0-D2	PLAW	yes	no	5.0	2%	—	5/3	10
EX-QPAR-G1.1	EXP	no	yes	—	—	QPAR <sup>e</sup>	1.1	10
EX-QPAR-G1.3	EXP	no	yes	—	—	QPAR	4/3	10
PL-QPAR-G1.1	PLAW	no	yes	—	—	QPAR	1.1	10
PL-QPAR-G1.3	PLAW	no	yes	—	—	QPAR	4/3	10
EX-ISO-G1.1	EXP	no	yes	—	—	ISO <sup>f</sup>	1.1	10
PL-ISO-G1.1	PLAW	no	yes	—	—	ISO	1.1	10
EX-C3.5-D1-QPAR-G1.3	EXP	yes	yes	3.5	1%	QPAR	4/3	10
EX-C3.5-D2-QPAR-G1.3	EXP	yes	yes	3.5	2%	QPAR	4/3	10
PL-C3.5-D1-QPAR-G1.3	PLAW	yes	yes	3.5	1%	QPAR	4/3	10
PL-C3.5-D2-QPAR-G1.3	PLAW	yes	yes	3.5	2%	QPAR	4/3	10
EX-C1.5-D1-2YR	EXP	yes	no	1.5	1%	—	5/3	5
EX-C5.0-D2-2YR	EXP	yes	no	5.0	2%	—	5/3	5

<sup>a</sup> Maximum perturbation of mass density; <sup>b</sup> percentage of the initial diameter of the remnant; <sup>c</sup> exponential profile; <sup>d</sup> power-law profile; <sup>e</sup> quasi-parallel injection; <sup>f</sup> isotropic injection.

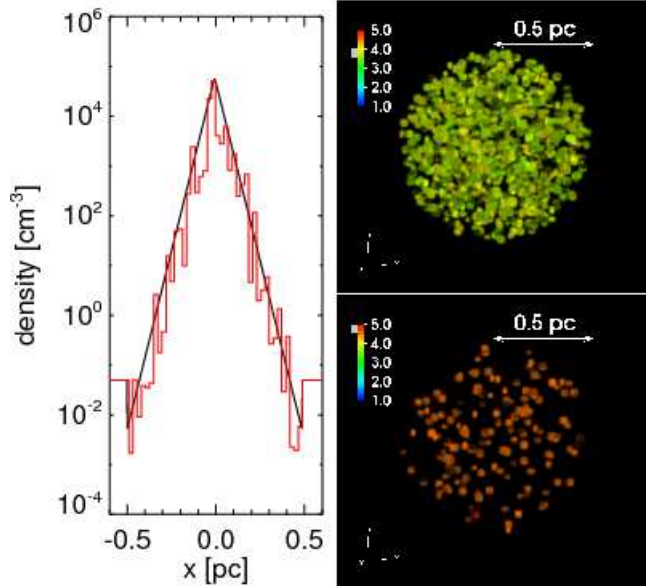


FIG. 2.— Left panel: initial spatial distribution of plasma density along the  $x$ -axis for a model either with (red line; run EX-C5.0-D2 in Table 1) or without (black line; run REF-EXP) the ejecta clumping. In both models the total mass of ejecta (integrated over the whole volume) is  $1.4 M_{\text{sun}}$  (see text). Right panels: initial spatial distributions of ejecta clumps with density perturbation in the range either  $[3.5 - 4]$  (upper panel) or  $[4.5 - 5]$  (lower panel) in run EX-C5.0-D2.

turbed magneto-static medium. Note that we paid particular attention to have an initial total mass of ejecta  $M_{\text{ej}} = 1.4 M_{\text{sun}}$  in all the simulations considered here, including those with a clumpy structure of the ejecta.

The initial total energy  $E_0 = 1.5 \times 10^{51}$  ergs leads to a remnant radius  $R_{\text{snr}} \approx 8.5$  pc at  $t = 1000$  yr and is partitioned so that  $> 99\%$  of the SN energy is kinetic. The remnant expands through a homogeneous isothermal medium of plasma number density  $n = 0.05 \text{ cm}^{-3}$  and temperature  $T = 10^4$  K. The initial ambient magnetic field configuration is that suggested by Bocchino et al. (2011) for SN 1006 and resulting from the comparison of radio observations of SN 1006 with MHD models: the ambient magnetic field is characterized by a non-zero gradient of its strength perpendicular to the average magnetic field that leads to a variation of  $|\vec{B}|$  of about a factor 1.4 over a scale of 10 pc. In all our simulations, the magnetic field strength is  $\approx 3 \mu\text{G}$  in the environment of the explosion site. We follow the remnant evolution for 1000 yr.

The computational domain extends 24 pc in the  $x$ ,  $y$ , and  $z$  directions. Special emphasis was placed on capturing the enormous range in spatial scales in the remnant. To this end, we exploited the adaptive mesh capabilities of the FLASH code by using 11 nested levels of resolution, with resolution increasing twice at each refinement level. The refinement/derefinement criterion adopted (Löhner 1987) follows the changes in mass density, temperature, and tracer of ejecta. In addition, the calculations were performed using also an automatic mesh derefinement scheme in the whole spatial domain that kept the computational cost approximately constant as the blast expanded: the maximum number of refinement levels used in the calculation gradually decreased from 11 (initially) to 7 (at the final time) following the expansion of the



blast and keeping roughly the same number of grid zones per radius of the remnant. At the beginning (at the end) of the simulation, this grid configuration yielded an effective resolution of  $\approx 2.9 \times 10^{-3}$  pc ( $\approx 4.6 \times 10^{-2}$  pc) at the finest level, corresponding to  $\approx 170$  zones per initial radius of the remnant ( $\approx 190$  zones per final radius of the remnant). The effective mesh size varied from  $8192^3$  initially to  $512^3$  at the final time.

We also performed two additional simulations with the same parameters of runs EX-C1.5-D1 and EX-C5.0-D2 but starting as early as  $\approx 2$  yr after the SN explosion (the initial spherical remnant has radius  $R_{\text{fs}0} = 0.125$  pc) to check if the results depend on the time when the clumpy structure of the ejecta is initialized. The results of this comparison are discussed in Appendix A.

### 3. RESULTS

#### 3.1. Effects of back-reaction of accelerated cosmic rays

As a first step, we analyzed the effects of back-reaction of accelerated CRs on the separation between the blast wave and the contact discontinuity, by considering models accounting for the shock modification by accelerated CR particles but without initial clumping of ejecta<sup>10</sup>. A recent comprehensive study of these effects on the development of RT instabilities in young SNRs is given by Wang (2011) (see also references therein). Our study differs from previous works in that it includes magnetic fields and a possible dependence of the CR particle acceleration on the obliquity angle. In particular, we focused on the isotropic and quasi-parallel scenario discussed in Sect. 2; the results for models assuming quasi-perpendicular injection are expected to be analogous to those discussed here for quasi-parallel injection, showing a modulation of the shock modification with the obliquity angle.

As expected for cases in which the magnetic field has a component parallel to the surface of the contact discontinuity (Chandrasekhar 1961), the magnetic field limits the growth of hydrodynamic instabilities through the tension of field lines which maintain a more laminar flow around the contact discontinuity. The energy losses to CRs at the forward shock lead to a greater shock compression ratio in all the cases examined (see also Blondin & Ellison 2001; Wang 2011). As a consequence, the density of the shocked ISM is greater and the separation between the blast wave and the contact discontinuity is shorter than predicted for a non-modified shock in regions with  $\gamma_{\text{eff}} < 5/3$ , i.e. where the back-reaction of accelerated CRs is efficient. In the quasi-parallel case, since the back-reaction of CRs is more effective at parallel shocks, the shock modification is modulated with the obliquity angle. As an example of this case, Fig. 3 presents the results for a model with an exponential profile of the initial ejecta density after 1000 yr of evolution (run EX-QPAR-G1.1; see Table 1). In this model we also assumed extreme energy losses to accelerate the CRs, so that the minimum effective adiabatic index is  $\gamma_{\text{eff}} = 1.1$ . The modulation of the back-reaction of accelerated CRs with the obliquity angle is evident in the figure, showing a larger compressibility and higher values of plasma den-

<sup>10</sup> Note that, in these simulations, we did not introduce any seed perturbation. The departures from spherical symmetry are entirely due to the mesh and to possible numerical fluctuations.

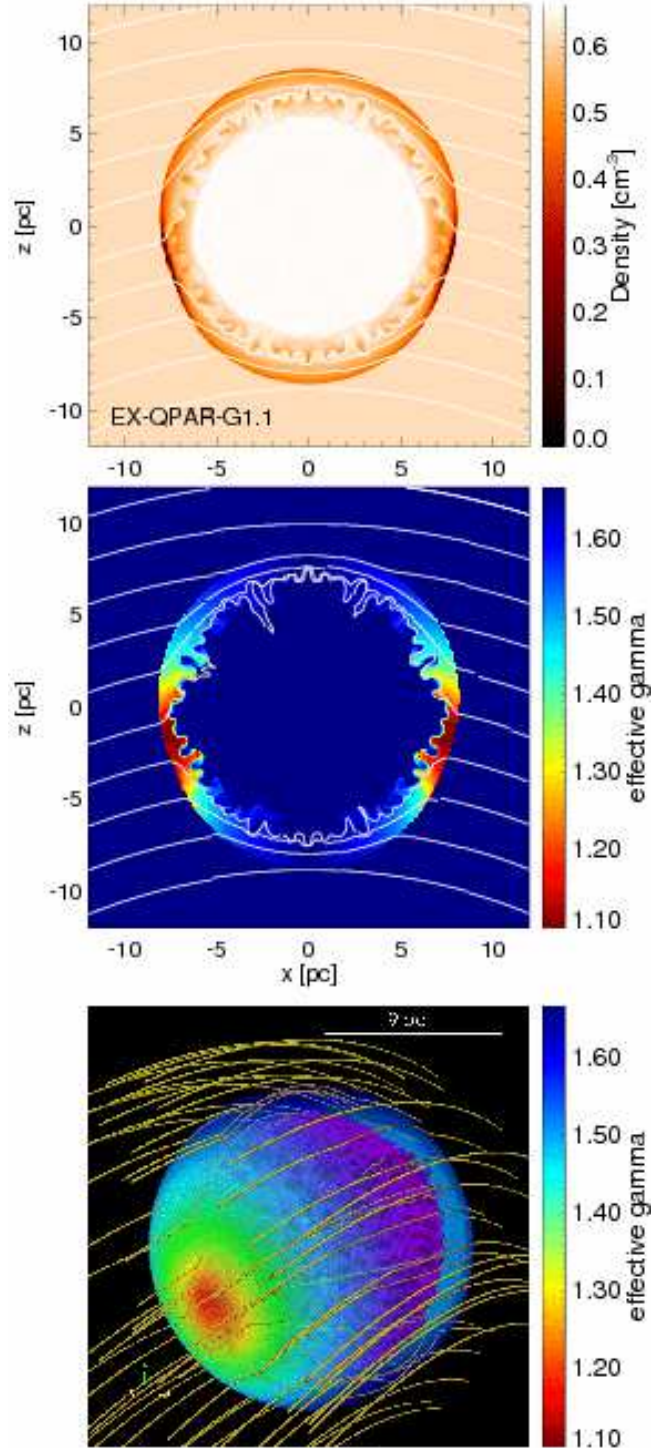


FIG. 3.— 2D sections in the  $(x, z)$  plane of the spatial distribution of plasma number density (upper panel) and effective adiabatic index (middle panel), after 1000 yr of evolution, for a model accounting for the shock modification by accelerated CRs but without initial clumping of ejecta (run EX-QPAR-G1.1). The lower panel shows the 3D volume rendering describing the spatial distribution of the effective adiabatic index. The index  $\gamma_{\text{eff}}$  is minimum in red regions (see colour bar). The white lines in the upper two panels and the yellow lines in the lower panel are sampled magnetic field lines. The violet surface in the lower panel tracks the ejecta material.

sity at parallel shocks. Such a modulation is absent in the isotropic case where the effects of CR particle acceleration are the same everywhere at the shock front

(runs EX-ISO-G1.1 and PL-ISO-G1.1). In these cases the plasma compressibility is the largest everywhere at the shock front, and the post-shock magnetic field can reach values up to  $\approx 50 - 70 \mu\text{G}$  at perpendicular shocks. It is worth mentioning that in both the quasi-parallel and isotropic cases, the simulations do not show any significant perturbation of the remnant outline and occurrence of protrusions after 1000 yr of evolution, even assuming extreme energy losses to accelerate the CRs. These results are in agreement with previous studies showing that enhanced RT mixing due to efficient particle acceleration determines only a slight perturbation of the forward shock near the epoch of young SNRs as SN 1006 or Tycho (e.g. Blondin & Ellison 2001; Wang 2011).

We investigated the effect of accelerated CRs on the separation between the blast wave and the contact discontinuity, by deriving the azimuthal profiles of the ratio of the forward shock radius to the contact discontinuity radius  $R_{\text{fs}}/R_{\text{cd}}$  from the models. The position of the forward shock was estimated from 2D maps of projected emission-measure-weighted temperature  $\langle T \rangle$  as the jump in  $\langle T \rangle$  in the direction of compression (determined by looking at the velocity field) at temperatures  $T > 1 \text{ MK}$ . The position of the contact discontinuity was estimated by using the passive tracer  $C_{\text{ej}}$  included in the model (see Sect. 2): during the remnant evolution, the ejecta and the shocked ISM mix together, leading to regions with  $0 < C_{\text{ej}} < 1$ ; at any time  $t$  the density of ejecta material in a fluid cell is given by  $\rho_{\text{ej}} = \rho C_{\text{ej}}$ . We derived the position of the contact discontinuity from 2D maps of projected  $\rho_{\text{ej}}$  as the local peak of  $\rho_{\text{ej}}$  closest to the forward shock in the direction of compression. The azimuthal profiles derived from the models in such a way are directly comparable with observations and, in particular, with the profiles derived by Miceli et al. (2009) in the analysis of the observations of SN 1006 (see Fig. 6 in Miceli et al. 2009).

Fig. 4 shows the azimuthal profiles of  $R_{\text{fs}}/R_{\text{cd}}$  derived from the models when the aspect angle is  $90^\circ$  (i.e. when the average magnetic field is perpendicular to the line of sight). The green line is the profile derived from the observations of SN 1006 (Miceli et al. 2009) and the black lines are the reference models with no shock modification and no ejecta clumping. The gray stripes mark the regions where, in the models, the acceleration of CRs is the largest. In the quasi-parallel case, we found that the modeled profiles are modulated by the obliquity angle and, in general, are higher than those observed (see red and blue lines in Fig. 4). The observations can be reproduced only in limited regions where the effect of accelerated CRs is the highest. Aspect angles lower than  $90^\circ$  make the comparison between models and observations worse because the regions of efficient CRs acceleration would not be at the limb (so that the ratio  $R_{\text{fs}}/R_{\text{cd}}$  increases). On the other hand, the models with no obliquity dependence of the back-reaction of accelerated CRs and  $\gamma_{\text{eff}} = 1.1$  reproduce the observed profiles quite well (magenta lines in Fig. 4). These results suggest that the observations could be reproduced only if the back-reaction of accelerated CRs is extreme (i.e.  $\gamma_{\text{eff}} \approx 1.1$ ) and independent of obliquity angle (i.e. the CRs acceleration and escape should be ubiquitous at the forward shock).

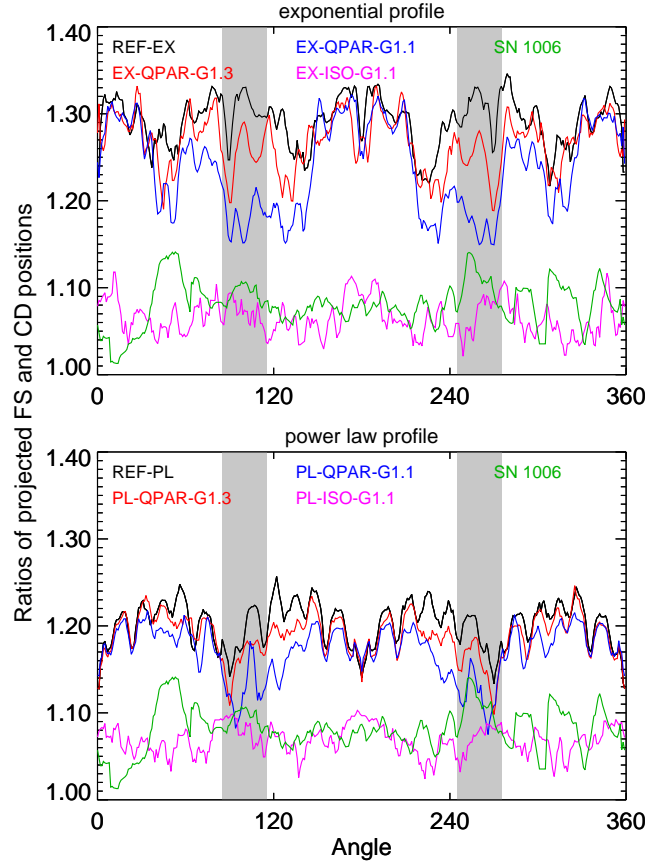


FIG. 4.— Azimuthal profiles of the ratio of the forward shock radius to the contact discontinuity radius  $R_{\text{fs}}/R_{\text{cd}}$  for models without ejecta clumping and with initial ejecta density profile either exponential (upper panel) or power-law (lower panel). The black lines mark the profiles derived from the reference models not accounting for the back-reaction of accelerated CRs (runs REF-EX and REF-PL). The red and blue lines mark the profiles derived from models including the shock modification modulated by the obliquity angle either with minimum  $\gamma_{\text{eff}} = 4/3$  (red lines; runs EX-QPAR-G1.3 and PL-QPAR-G1.3) or minimum  $\gamma_{\text{eff}} = 1.1$  (blue lines; runs EX-QPAR-G1.1 and PL-QPAR-G1.1). The magenta lines mark the profiles derived from models including the shock modification with no obliquity dependence and  $\gamma_{\text{eff}} = 1.1$  (runs EX-ISO-G1.1 and PL-ISO-G1.1). The green line marks the profile derived from the observations of SN 1006 (Miceli et al. 2009). The gray stripes mark the regions where the acceleration of CRs is the largest.

### 3.2. Effects of ejecta clumping and instability

As a next step, we investigated the effects of ejecta clumping on the evolution and morphology of the remnant by considering models without back-reaction of accelerated CRs and accounting only for the ejecta clumping. In addition to the spectropolarimetric studies of SNe discussed in Sect. 1 (see also Hole et al. 2010 and references therein), a widespread clumpiness of ejecta is also suggested by X-ray and radio observations, showing knots located near the edge of the remnants, and outward protrusions in many cases surrounding the knots (e.g. Hwang & Gotthelf 1997; Velazquez et al. 1998; Rakowski et al. 2011). All these features cannot be explained by instabilities generated by linear perturbations and have been interpreted as being due to clumps of ejecta expanding into the intershock region (e.g. Wang & Chevalier 2001). The interactions among the clumps of ejecta are expected to contribute to seed the RT instabilities and enhance their growth, thus strongly



influencing the final morphology of the remnant.

The basic physics of the evolution of a single clump of ejecta expanding through the intershock structure of a SNR is similar to that for the interaction of a shock with a cloud of the ISM (e.g. Klein et al. 1994) and has been extensively discussed by Wang & Chevalier (2001). The major factors in the clump-remnant interaction are the density contrast of the clump with respect to the ISM, the clump size, and the position of the clump in the initial distribution of ejecta (or, alternatively, the time of initiation of the clump-shock interaction). In general, after passing through the reverse shock, the single clump evolves toward a core-plume structure with a crescent-like shape characterized by Kelvin-Helmholtz (KH) instabilities developing in the downstream region. As the clump travels through the intershock structure, RT instabilities develop on the upstream side of the clump, leading to its progressive fragmentation. Depending on its initial density contrast, size, and time of initiation of the clump-shock interaction, the clump can reach the forward shock, causing a bulge on the remnant outline as the ram pressure pushes material ahead (see Wang & Chevalier 2001 for a detailed description). This is the way ejecta protrusions form. After the clump is completely fragmented, the bulge (the protrusion) disappears and the clump fragments are mixed with the shocked ISM and swept back in the remnant. The perturbation of the forward shock front by the interaction with the clumps is more likely during the early phases of the remnant evolution when the density contrast between the ejecta clumps and the ISM is larger.

In our case, we are assuming that the ejecta structure is formed by hundreds of thousands of clumps modelled as per-cell random density perturbations (see Sect. 2 and Fig. 2); in each simulation, the clumps have the same size and are characterized by different density contrasts (i.e. different density perturbations) and different positions (i.e. the time of initiation of the interaction of each clump with the reverse shock is different). The clump-remnant interaction therefore is complicated by the multiple interactions among clumps with different density contrast and velocity. In addition, our model includes the magnetic field which is known to limit the growth of hydrodynamic instabilities in the shock-cloud interaction (e.g. Mac Low et al. 1994; Jones et al. 1996) due to the tension of the magnetic field lines which maintain a more laminar flow around the cloud surface (see also Fragile et al. 2005; Orlando et al. 2008). In the present case, during the clump evolution, the magnetic field is expected to be trapped at the nose of the clump, leading to a continuous increase of the magnetic pressure and field tension there that limit the growth of RT instabilities responsible for the clump fragmentation. As a result, the clumps are expected to survive for a longer time than those studied by Wang & Chevalier (2001) (their simulations do not include the magnetic field), increasing their probability to reach the forward shock.

As an example, Fig. 5 shows a close-up view of the remnant limb for the model EX-C5.0-D2, illustrating the magnetic field strength (upper panel) and the plasma density distribution (lower panel) at  $t = 1000$  yr. As expected, the magnetic field follows the plasma structures formed during the evolution of the clumps with preferentially radial components around the RT fingers.

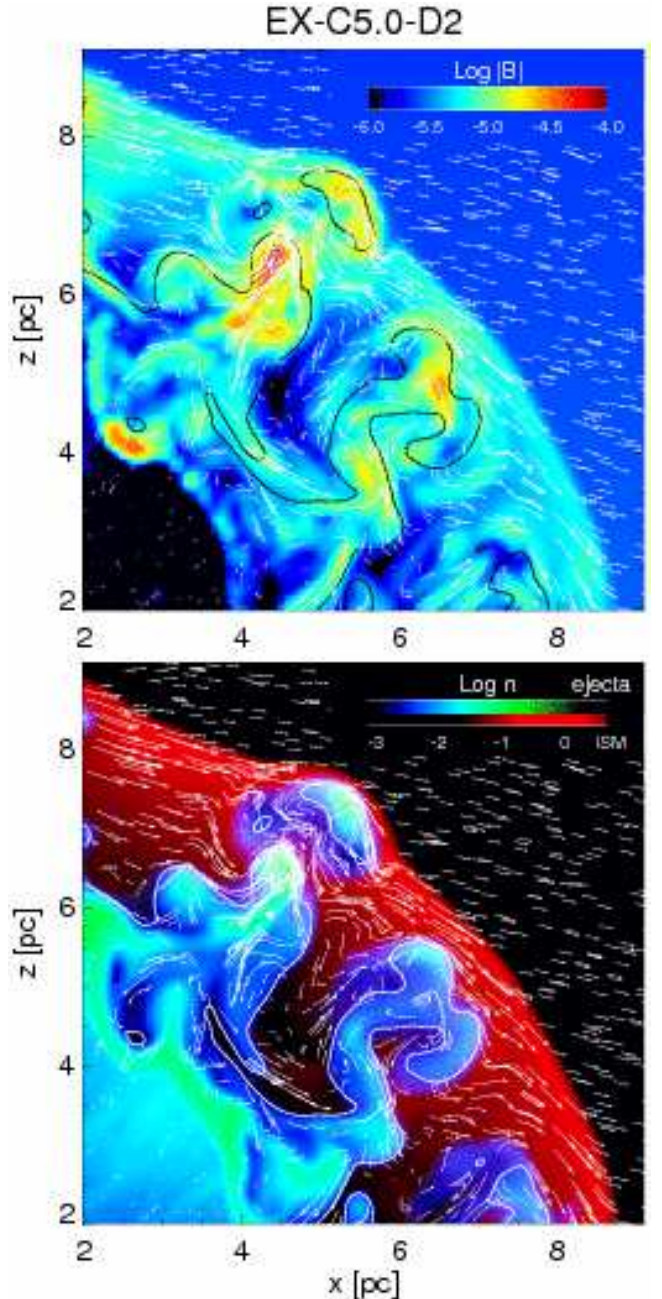


FIG. 5.— Close-up view of the remnant limb for the model EX-C5.0-D2 at  $t = 1000$  yr, showing a colour-coded cross-section image of the magnetic field strength (G; upper panel) and a composite cross-section image (lower panel) combining the plasma density ( $\text{cm}^{-3}$ ) of the shocked ISM (red) and that of the ejecta (blue-green). The contours enclose the cells consisting of the original ejecta material by more than 10%. The magnetic field is described by the superimposed arrows the length of which is proportional to the magnitude of the field vector.

The magnetic field is strongly modified by the clumps and it can be enhanced by up to two orders of magnitude ( $|\vec{B}| \approx 100 \mu\text{G}$ , whereas the unperturbed magnetic field strength is  $\approx 2.5 \mu\text{G}$ ) in the ejecta clumps (see red regions in the upper panel of Fig. 5). Note that, in model EX-C5.0-D2, no back-reaction of accelerated CRs is taken into account and the magnetic field in inter-clumps regions at the forward shock ( $|\vec{B}| \approx 10 \mu\text{G}$ ) is that predicted for non-modified shocks, namely much lower than that measured in the X-ray rims of

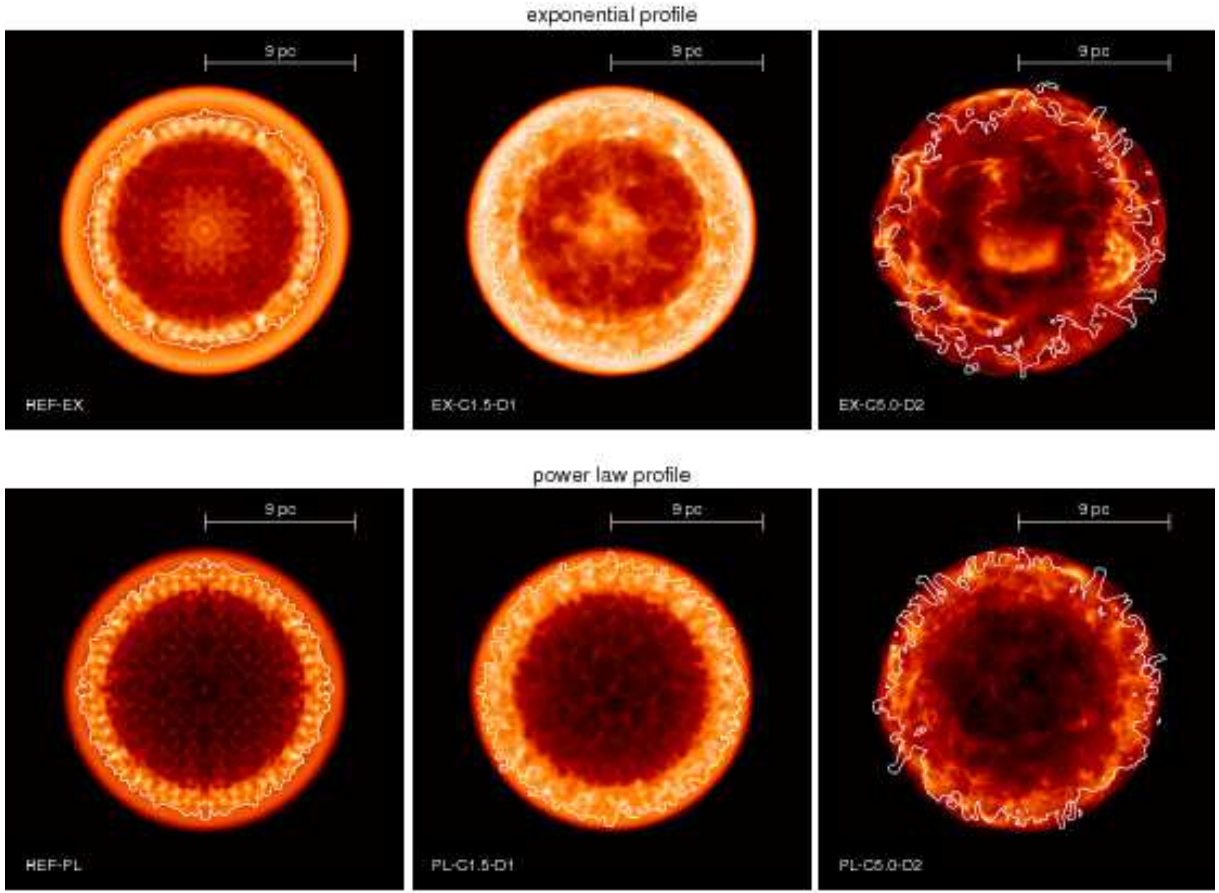


FIG. 6.— 3D rendering of mass density for models with an exponential (upper panels) or a power-law (lower panels) initial profile of ejecta and no shock modification by CRs, after 1000 yr of evolution. Left panels show the maps derived from the reference models not including the ejecta clumping (runs REF-EX and REF-PL). The initial clumpy structure of the ejecta is characterized by clumps either with size  $\approx 1\%$  of the initial diameter of the remnant  $D_{\text{snr}0}$  and maximum density perturbation  $\nu_{\text{max}} = 1.5$  (center panels) or with size  $\approx 2\%$  of the initial diameter of the remnant and maximum density perturbation  $\nu_{\text{max}} = 5.0$  (right panels). The white contours enclose the ejecta material (i.e. cells consisting of the original ejecta material by more than 50%).

SN 1006 ( $50 \lesssim |\vec{B}| \lesssim 150 \mu\text{G}$ ; Berezhko et al. 2003, 2009; Acero et al. 2010; Petruk et al. 2011, 2012).

As examples, Fig. 6 shows the 3D rendering of plasma density for the reference cases without clumping (runs REF-EX and REF-PL) and for the limit cases with clumping considered in this paper, namely models with an ejecta structure characterized either by clumps with small size and low density perturbations (runs EX-C1.5-D1 and PL-C1.5-D1 in Table 1) or by clumps with large size and high density perturbations (runs EX-C5.0-D2, and PL-C5.0-D2). The figure shows that the enhanced intershock RT mixing can easily spread the ejecta material close to, or even beyond, the average radius of the forward shock, depending on the size and density contrast of the initial clumps. This can occur very soon after the explosion, depending again on the size and density contrast of the clumps seeding the instabilities. As a result, we found that: 1) the RT mixing reaches the forward shock front possibly perturbing the remnant outline, 2) knots and filamentary structures characterize the remnant morphology, and 3) clumps of ejecta can be very close to or even protruding beyond the main blast wave leading to evident knots near the remnant edge as observed, for instance, in SN 1006 (Rakowski et al. 2011) and Tycho’s SNR (e.g. Velazquez et al. 1998). In general, increasing the initial size of the clumps or their den-

sity perturbation (i.e. going from the left to the right panel of Fig. 6), both the perturbation of the remnant outline and the occurrence of ejecta protrusions increase. Fig. 6 also shows that the characteristic size of the density features formed within the remnant is comparable to that of the features observed, for instance, in SN 1006.

A remarkable feature of the simulations including the ejecta clumping is the occurrence of several protrusions due to clumps of ejecta overtaking the forward shock. Fig. 7 shows composite images of the SNR combining the square of plasma density of the shocked ISM (red) and that of the ejecta (green and yellow), both projected along the line-of-sight, for models EX-C5.0-D2 and PL-C5.0-D2. The protrusions are evident in both cases and are due to clumps with high density contrast originating from the outer layers of the ejecta. Our calculations show that the number of protrusions at  $t = 1000$  yr is higher for larger size of the clumps and higher density contrasts of the clumps and decreases with the age of the remnant. In fact the simulations showed that, during the remnant evolution, new protrusions are continuously formed and, subsequently, disappear when the clumps responsible for them are decelerated and the forward shock front catches up with them (see also Wang & Chevalier 2002). In this process, the clumps contribute in the perturbation of the remnant outline and in the formation of plasma features



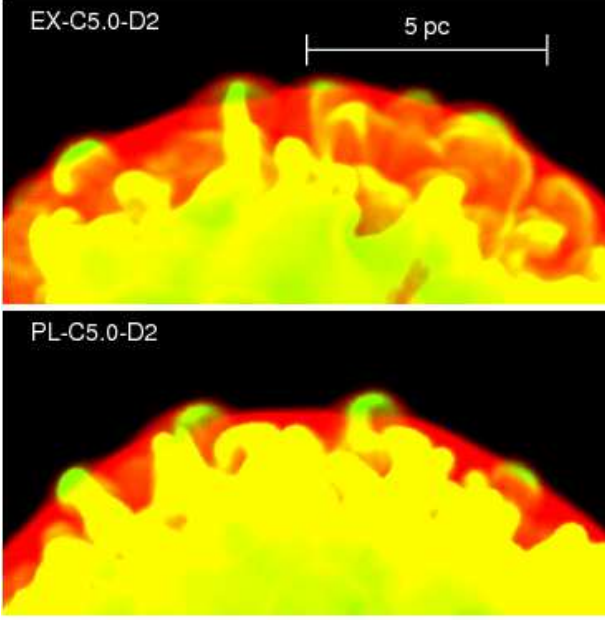


FIG. 7.— Composite images of the remnant limb showing the square of plasma density of the shocked ISM (red) and that of the ejecta (green and yellow), both projected along the line-of-sight, for models EX-C5.0-D2 (upper panel) and PL-C5.0-D2 (lower panel) after 1000 yr of evolution.

in the outer part of the remnant.

Also in this case, we compared the azimuthal profiles of the ratio  $R_{fs}/R_{cd}$  derived from the models with that observed in SN 1006 (see Fig. 8). We found that the initial clumping of ejecta makes the azimuthal profiles of  $R_{fs}/R_{cd}$  fairly uniform and lower than expected for models without a clumpy structure of the ejecta and comparable with models accounting for extreme and ubiquitous acceleration of CR particles at the forward shock (i.e. isotropic models with  $\gamma_{eff} \approx 1.1$ ; compare Fig. 4 and Fig. 8). In particular, we found that, in the case of SN 1006, the observed profile can be reproduced by models with a maximum density perturbation of ejecta  $\nu_{max}$  ranging between 2.5 and 5, and with initial size of ejecta clumps of the order of 2% of the initial diameter of the remnant (see the blue lines in middle and lower panels in Fig. 8).

### 3.3. Ejecta clumping and cosmic rays acceleration

As a last step, we have investigated the effects of back-reaction of accelerated CRs on the remnant morphology in the presence of ejecta clumping through simulations including both physical processes (runs EX-C3.5-D1-QPAR-G1.3, EX-C3.5-D2-QPAR-G1.3, PL-C3.5-D1-QPAR-G1.3, and PL-C3.5-D2-QPAR-G1.3 in Table 1). We found that when the CR acceleration efficiency depends on the obliquity angle (e.g. quasi-parallel models), the modulation of the shock modification with the obliquity angle is not appreciable in the presence of ejecta clumping (see Fig. 9). In other words, our model predict that the ejecta clumping can wash out the CR back-reaction effects on the separation between the forward shock and the contact discontinuity. On the other hand, our simulations have shown that the effects of back-reaction of accelerated CRs can still be visible on the azimuthal profile of plasma density which shows local maxima where the acceleration of CRs is the largest (the

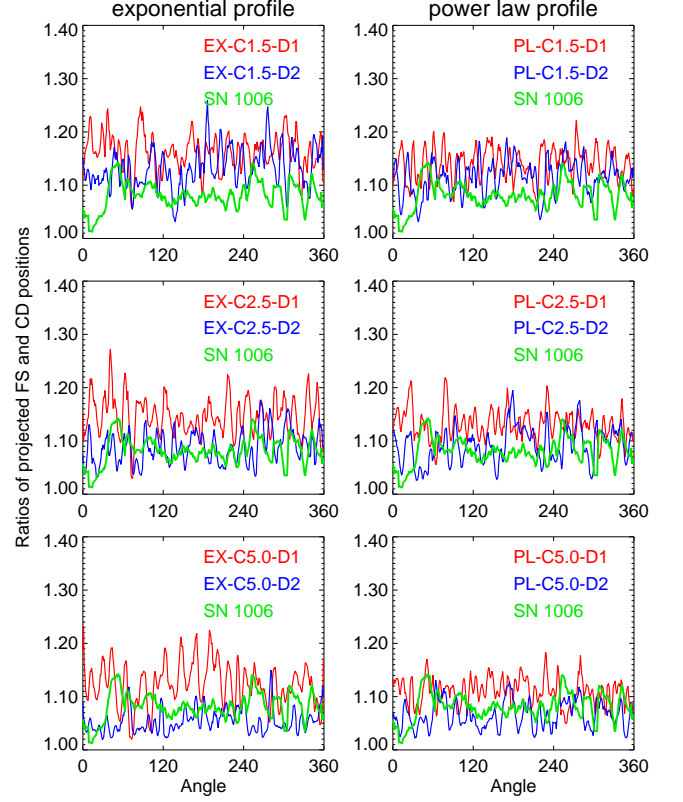


FIG. 8.— Azimuthal profiles of the ratio of the forward shock radius to the contact discontinuity radius  $R_{fs}/R_{cd}$  for models without back-reaction of accelerated CRs and with ejecta clumping and initial ejecta density profile either exponential (left panels) or power-law (right panels). The figure shows the profiles derived from models with maximum density perturbation  $\nu_{max} = 1.5$  (upper panels),  $\nu_{max} = 2.5$  (middle), and  $\nu_{max} = 5.0$  (lower), and with initial size of the clumps  $\approx 1\%$  (red lines) and  $\approx 2\%$  (blue lines) of the initial diameter of the remnant  $D_{snr0}$ . The green line marks the profile derived from the observations of SN 1006 (Miceli et al. 2009).

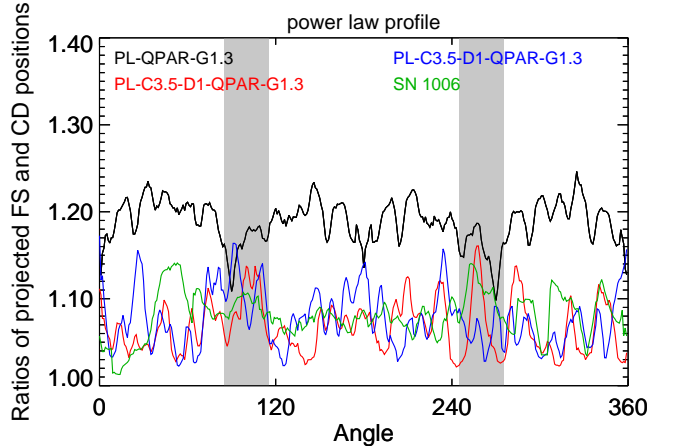


FIG. 9.— As in Fig. 4 for a model accounting for the back-reaction of accelerated CRs only (run PL-QPAR-G1.3) and for models including both the CR particle acceleration and the ejecta clumping (runs PL-C3.5-D1-QPAR-G1.3, and PL-C3.5-D2-QPAR-G1.3). In all the cases, the minimum  $\gamma_{eff} = 4/3$ . The green line marks the profile derived from the observations of SN 1006 (Miceli et al. 2009). The gray stripes mark the regions where the acceleration of CRs is the largest.

plasma compressibility being the highest there).

To make a more quantitative comparison between the

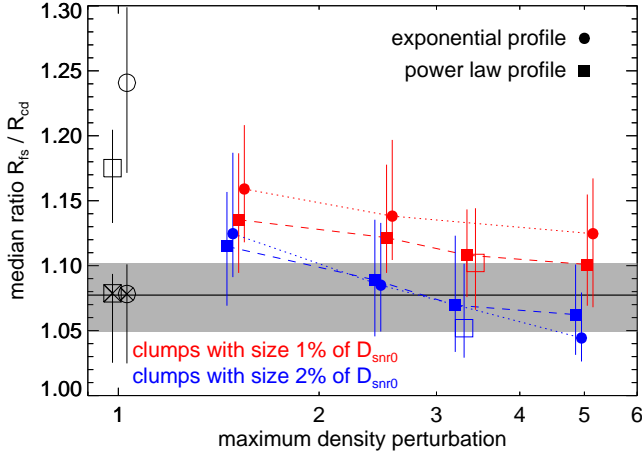


FIG. 10.— Median values of the ratio of the forward shock radius to the contact discontinuity radius  $R_{fs}/R_{cd}$  versus the maximum density perturbation  $\nu_{max}$  for models either with (red and blue symbols for initial size of the clumps  $\approx 1\%$  and  $\approx 2\%$  of the remnant diameter  $D_{snr0}$ , respectively) or without (black symbols) ejecta clumping, and for models including the back-reaction of accelerated CRs (empty and crossed symbols for the quasi-parallel and isotropic cases, respectively). The grey region marks the range of values observed in SN 1006 (Miceli et al. 2009).

model results and the observations, we derived the median values of  $R_{fs}/R_{cd}$  for each of the models in Table 1 and for the observed profile. Fig. 10 shows the median values of  $R_{fs}/R_{cd}$  versus the maximum density perturbation  $\nu_{max}$  for models accounting for only one of the effects considered in this paper (either back-reaction of accelerated CRs or ejecta clumping) and for models including both physical effects. We found that: the larger the size of initial clumps of ejecta, the lower the value of the median ratio; the higher the initial density perturbation, the lower the value of the median ratio. The back-reaction of accelerated CRs slightly reduces the value of the ratio in models accounting for the clumpy structure of the ejecta (empty symbols in Fig. 10) unless the energy losses to CRs are large with an effective adiabatic index  $\approx 1.1$  and ubiquitous at the forward shock (as in the isotropic injection, see models EX-ISO-G1.1 and PL-ISO-G1.1; crossed symbols in Fig. 10).

#### 4. SUMMARY AND CONCLUSIONS

We investigated the role of ejecta clumping and back-reaction of accelerated CRs on the evolution and morphology of young Type Ia SNRs and, in particular, on determining the observed separation between the forward shock and the contact discontinuity and the high occurrence of protrusions. To this end, we developed a 3D MHD model describing the expansion of the remnant through a medium with nonuniform interstellar magnetic field, including consistently the back-reaction of accelerated CRs and the initial clumpy structure of the ejecta. We explored two complementary cases in which one or the other of these physical processes is turned either on or off in order to identify its effects on the remnant evolution and morphology. Then we compared the model results with the observations of SN 1006 (Miceli et al. 2009). Particular attention has been devoted to perform simulations with sufficient spatial resolution to capture the details of the evolution of the clumps of ejecta, exploiting the adaptive mesh refinement capabilities of the FLASH code.

As expected, we found that the acceleration of CR particles makes the shell of shocked ISM thinner at the forward shock, thus reducing the separation between the forward shock and the contact discontinuity. Any dependence of the back-reaction of accelerated CRs on the obliquity angle should be evident as a modulation of the azimuthal profile of the ratio of the forward shock radius to the contact discontinuity radius  $R_{fs}/R_{cd}$ . In the case of SN 1006, the comparison of the modelled profiles with those observed shows that the back-reaction of accelerated CRs may reproduce the observations only if the energy losses to CRs are extreme (i.e. the effective adiabatic index is  $\gamma_{eff} \approx 1.1$ ) and independent of the obliquity angle (i.e. the effects of CR acceleration are ubiquitous at the forward shock). In addition, the simulations have shown that the large compression ratio due to the acceleration of CR particles has no significant effect on the growth of RT instabilities, in agreement with previous studies (e.g. Blondin & Ellison 2001; Frascchetti et al. 2010; Wang 2011). As a result, the remnant outline is only slightly perturbed by the instabilities with very few (if any) occurrence of protrusions near the epoch of young SNRs as SN 1006 or Tycho’s SNR, even with very efficient acceleration of CRs (see also Wang 2011). This fact contrasts with the evidence of several protrusions observed in SN 1006 (e.g. Rakowski et al. 2011) and Tycho’s SNR (e.g. Hwang & Gotthelf 1997; Velazquez et al. 1998).

On the other hand, the clumpy structure of the ejecta can have important consequences on the structure of the intershock RT mixing and on the final morphology of the remnant. In particular, we found that the ejecta clumps with the higher density contrasts approaching the contact discontinuity enhance the growth of RT instabilities; RT fingers can easily reach the forward shock and ejecta clumps can be found very close to, or even beyond, the average shock radius with no need to invoke any CR back-reaction at all to explain this phenomenon. As a result, the separation between the forward shock and the contact discontinuity can be significantly reduced, depending on the size and density contrast of the clumps. In particular, we found that the larger the size of initial clumps of ejecta and/or the higher their density contrast, the shorter the width of the interaction region between the forward shock and the contact discontinuity. The modelled azimuthal profile of  $R_{fs}/R_{cd}$  is fairly uniform as observed in SN 1006; the comparison of the model results with the observations of SN 1006 showed that the observed profile of  $R_{fs}/R_{cd}$  can be reproduced by models with a maximum density perturbation of ejecta  $\nu_{max}$  ranging between 2.5 and 5, and with initial size of ejecta clumps of the order of 2% of the initial diameter of the remnant. We also found that the remnant outline can be significantly perturbed by the enhanced RT fingers and, in case of high density contrasts and large size of the clumps, several protrusions can characterize the morphology of the remnant at the age of SN 1006. Our study supports the idea that enhanced RT mixing due to ejecta clumping can be responsible for the filamentary structures and bumps seen on the outlines of young SNRs as SN 1006 and Tycho’s SNR.

Finally, our analysis has shown that the ejecta clumping, if present, may wash out the effects of back-reaction of accelerated CRs on the separation between the for-

ward shock and the contact discontinuity. In particular, if the CR acceleration efficiency depends on the obliquity angle as, for instance, in the quasi-parallel scenario, the modulation of the shock modification with the obliquity angle may be not appreciable in the presence of ejecta clumping. We conclude therefore that, in general, the separation between the forward shock and the contact discontinuity is not a reliable diagnostic tool for studying the CR shock modification.

On the contrary, our model predicts that the effects of back-reaction of accelerated CRs can still be appreciable on the azimuthal profile of plasma density. In fact our simulations have shown that, even in the presence of ejecta clumping, the density profile has local maxima where the acceleration of CRs is the largest (the plasma compressibility being the highest there). Also, due to the enhanced plasma compressibility, the magnetic field strength can reach values of  $\approx 50 - 70 \mu\text{G}$  where the CR acceleration is the largest (see Sect. 3.1), that are comparable with those observed in the X-ray rims of SN 1006 (e.g. Berezhko et al. 2003, 2009; Acero et al. 2010; Petruk et al. 2011, 2012). It is interesting to note however that similar values of magnetic field strength can

also be reached locally in ejecta clumps close to the forward shock with no need to invoke any CR back-reaction, but as a result of the propagation of the clumps through the intershock region (see Fig. 5).

We thank an anonymous referee for useful suggestions. This work was supported in part by the Italian Ministry of University and Research (MIUR) and by Istituto Nazionale di Astrofisica (INAF). The software used in this work was in part developed by the DOE-supported ASC / Alliance Center for Astrophysical Thermonuclear Flashes at the University of Chicago. We acknowledge the CINECA Awards N. 998NZ7YK,2010 and N. HP10C7MTR0,2011 for the availability of high performance computing resources and support. Additional computations were carried out at the SCAN<sup>11</sup> (Sistema di Calcolo per l'Astrofisica Numerica) facility for high performance computing at INAF – Osservatorio Astronomico di Palermo. This work was partially funded by the ASI-INAF contract n. I/009/10/0.

<sup>11</sup> [http://www.astropa.unipa.it/progetti\\_ricerca/HPC/index.html](http://www.astropa.unipa.it/progetti_ricerca/HPC/index.html)

## REFERENCES

- Acero, F. et al. 2010, *A&A*, 516, A62  
 Berezhko, E. G., Ksenofontov, L. T., & Völk, H. J. 2003, *A&A*, 412, L11  
 —. 2009, *A&A*, 505, 169  
 Blondin, J. M., & Ellison, D. C. 2001, *ApJ*, 560, 244  
 Bocchino, F., Orlando, S., Miceli, M., & Petruk, O. 2011, *A&A*, 531, A129+  
 Cassam-Chenaï, G., Hughes, J. P., Ballet, J., & Decourchelle, A. 2007, *ApJ*, 665, 315  
 Chandrasekhar, S. 1961, *Hydrodynamic and hydromagnetic stability* (International Series of Monographs on Physics, Oxford: Clarendon, 1961)  
 Chevalier, R. A. 1977, *ARA&A*, 15, 175  
 —. 1983, *ApJ*, 272, 765  
 Chornock, R., & Filippenko, A. V. 2008, *AJ*, 136, 2227  
 Dwarkadas, V. V., & Chevalier, R. A. 1998, *ApJ*, 497, 807  
 Ellison, D. C., Decourchelle, A., & Ballet, J. 2004, *A&A*, 413, 189  
 —. 2005, *A&A*, 429, 569  
 Ferrand, G., Decourchelle, A., Ballet, J., Teyssier, R., & Frascchetti, F. 2010, *A&A*, 509, L10  
 Fragile, P. C., Anninos, P., Gustafson, K., & Murray, S. D. 2005, *ApJ*, 619, 327  
 Franco, J., Miller, III, W. W., Arthur, S. J., Tenorio-Tagle, G., & Terlevich, R. 1994, *ApJ*, 435, 805  
 Frascchetti, F., Teyssier, R., Ballet, J., & Decourchelle, A. 2010, *A&A*, 515, A104+  
 Fryxell, B. et al. 2000, *ApJS*, 131, 273  
 Fulbright, M. S., & Reynolds, S. P. 1990, *ApJ*, 357, 591  
 Hole, K. T., Kasen, D., & Nordsieck, K. H. 2010, *ApJ*, 720, 1500  
 Hwang, U., & Gotthelf, E. V. 1997, *ApJ*, 475, 665  
 Jones, T. W., Ryu, D., & Tregillis, I. L. 1996, *ApJ*, 473, 365  
 Klein, R. I., McKee, C. F., & Colella, P. 1994, *ApJ*, 420, 213  
 Leonard, D. C., Li, W., Filippenko, A. V., Foley, R. J., & Chornock, R. 2005, *ApJ*, 632, 450  
 Löhner, R. 1987, *Comp. Meth. Appl. Mech. Eng.*, 61, 323  
 Mac Low, M., McKee, C. F., Klein, R. I., Stone, J. M., & Norman, M. L. 1994, *ApJ*, 433, 757  
 MacNeice, P., Olson, K. M., Mobarrry, C., de Fainchtein, R., & Packer, C. 2000, *Comp. Phys. Comm.*, 126, 330  
 Maeda, K. et al. 2010a, *Nature*, 466, 82  
 Maeda, K., Röpke, F. K., Fink, M., Hillebrandt, W., Travaglio, C., & Thielemann, F.-K. 2010b, *ApJ*, 712, 624  
 Mansfield, V. N., & Salpeter, E. E. 1974, *ApJ*, 190, 305  
 Miceli, M. et al. 2009, *A&A*, 501, 239  
 Nomoto, K., Thielemann, F.-K., & Yokoi, K. 1984, *ApJ*, 286, 644  
 Orlando, S., Bocchino, F., Reale, F., Peres, G., & Pagano, P. 2008, *ApJ*, 678, 274  
 Orlando, S., Bocchino, F., Reale, F., Peres, G., & Petruk, O. 2007, *A&A*, 470, 927  
 Orlando, S., Petruk, O., Bocchino, F., & Miceli, M. 2011, *A&A*, 526, A129+  
 Petruk, O., Beshley, V., Bocchino, F., Miceli, M., & Orlando, S. 2011, *MNRAS*, 413, 1643  
 Petruk, O., Kuzyo, T., & Bocchino, F. 2012, *MNRAS*, 419, 608  
 Rakowski, C. E., Laming, J. M., Hwang, U., Eriksen, K. A., Ghavamian, P., & Hughes, J. P. 2011, *ApJ*, 735, L21+  
 Truelove, J. K., & McKee, C. F. 1999, *ApJS*, 120, 299  
 Velazquez, P. F., Gomez, D. O., Dubner, G. M., de Castro, G. G., & Costa, A. 1998, *A&A*, 334, 1060  
 Völk, H. J., Berezhko, E. G., & Ksenofontov, L. T. 2003, *A&A*, 409, 563  
 Wang, C.-Y. 2011, *MNRAS*, 415, 83  
 Wang, C.-Y., & Chevalier, R. A. 2001, *ApJ*, 549, 1119  
 —. 2002, *ApJ*, 574, 155  
 Wang, L. et al. 2003, *ApJ*, 591, 1110  
 Wang, L., Baade, D., Höflich, P., Wheeler, J. C., Kawabata, K., Khokhlov, A., Nomoto, K., & Patat, F. 2006, *ApJ*, 653, 490  
 Wang, L., Baade, D., Höflich, P., Wheeler, J. C., Kawabata, K., & Nomoto, K. 2004, *ApJ*, 604, L53  
 Warren, J. S. et al. 2005, *ApJ*, 634, 376



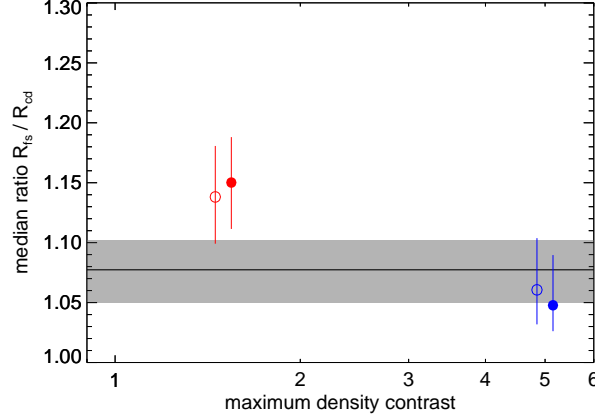


FIG. A1.— As in Fig. 10 for models starting as early as either  $\approx 2$  yr (empty symbols; runs EX-C1.5-D1-2YR and EX-C5.0-D2-2YR) or  $\approx 10$  yr (filled symbols; runs EX-C1.5-D1, EX-C5.0-D2) after the SN explosion. Red and blues symbols show the results for models with initial size of the clumps  $\approx 1\%$  and  $\approx 2\%$  of the remnant diameter  $D_{\text{snr}0}$ , respectively. The grey region marks the range of values observed in SN 1006 (Miceli et al. 2009).

## APPENDIX

### DEPENDENCE OF THE RESULTS ON THE INITIAL CONDITIONS

We checked the dependence of the results on the initial conditions and in particular on the time when the clumpy structure of the ejecta is initialized. To this end, we performed two additional simulations (runs EX-C1.5-D1-2YR and EX-C5.0-D2-2YR in Table 1) with the same parameters of runs EX-C1.5-D1 and EX-C5.0-D2 but starting as early as  $\approx 2$  yr after the SN explosion (i.e. the initial spherical remnant has radius  $R_{\text{fs}0} = 0.125$  pc) instead of  $\approx 10$  yr (with  $R_{\text{fs}0} = 0.5$  pc). In other words, we checked the dependence of the results on the initial conditions for the limit cases considered in this paper, namely models with a clumpy structure of the ejecta characterized either by clumps with small size and low density perturbations (run EX-C1.5-D1) or by clumps with large size and high density perturbations (run EX-C5.0-D2). For runs EX-C1.5-D1-2YR and EX-C5.0-D2-2YR, we used 13 nested levels of resolution in the automatic mesh derefinement scheme to keep the same spatial resolution as the other simulations discussed here (i.e. 172 zones per initial radius of the remnant); in this case the effective mesh size was  $32768 \times 32768 \times 32768$ .

From the additional simulations, we derived the azimuthal profile of the ratio of the forward shock radius to the contact discontinuity radius  $R_{\text{fs}}/R_{\text{cd}}$  as done for the other runs (see Fig. 8); then, from these profiles, we derived the median values of  $R_{\text{fs}}/R_{\text{cd}}$  and compared them with those derived from runs EX-C1.5-D1 and EX-C5.0-D2 (see Fig. A1). In both cases analyzed, with ejecta clumps with either small size and low density perturbations or large size and high density perturbations (namely the two limit cases explored in this paper), we found that the median values of  $R_{\text{fs}}/R_{\text{cd}}$  derived from models with different initial ages are consistent within the error bars, the value being slightly lower (higher) in the model with initial age of the remnant  $t_{\text{snr}0} = 2$  yr than in the model with  $t_{\text{snr}0} = 20$  yr when the clump size is 1% (2%) and the maximum density perturbation is  $\nu = 1.5$  ( $\nu = 5$ ). We conclude therefore that the results presented here do not depend on the initial age of the simulated remnant. Indeed our results undoubtedly show that the average separation between the contact discontinuity and the forward shock strongly depends on the clumpy structure of the ejecta and, in particular, on the size and density contrasts of the clumps.